From Master equation to SPICE: a platform to model cryo-CMOS control for qubits

Vladimir Pešić
AQUA Lab
EPFL Neuchâtel, Switzerland
vladimir.pesic@epfl.ch

Andrew Wright
AQUA Lab
EPFL Neuchâtel, Switzerland
andrew.wrightgarcia@epfl.ch

Edoardo Charbon
AQUA Lab &Center for Quantum Science and Engineering
EPFL Neuchâtel, Switzerland
edoardo.charbon@epfl.ch

***Abstract*—Cryogenic classical electronics for the control of qubits can be placed near quantum processors for a more compact system, ultimately enabling a highly scalable one. However, cryogenic operation poses very strict power requirements on electronics, in addition to heavy constraints on precision in both amplitude and phase, as well as noise, so as to achieve the necessary fidelity. To test all the trade-offs that arise from these requirements, detailed simulations based on the physics of qubits and on the effects that circuits may have on them are needed. This paper focuses on the models and the simulation framework needed for quantum processors that can be efficiently executed on classical hardware. These models allow circuit design and specification derivation at all levels of the design. The suitability of the approach is demonstrated with superconducting qubit platforms and their control and characterization.**

***Index Terms*—Cryo-CMOS, superconducting qubits, cQED, qubit control, specifications**

I. Introduction

Superconducting qubit platforms exhibit promising potential in realizing a quantum computer with many qubits and diverse functionality. However, in most embodiments, superconducting circuits require the quantum processor to operate inside a dilution refrigerator, while most of its interface is placed outside operating at room temperature (RT) [1]. This approach limits the potential for further scaling of quantum systems due to interconnect complexity between the mK stage and RT instruments. To address this issue, the use of cryogenic complementary metal-oxide semiconductor electronics (cryo-CMOS) for control and readout placed inside the refrigerator has been proposed [2], [3].

Cryogenic interface electronics offers a solution to a few important issues that influence scalability. First of all, systems with room-temperature setups need complex cabling to connect qubits with outside electronics, which presents a bottleneck to the number of qubits that can reasonably be handled and, most importantly, to the reliability of the system, thus making it hard to debug and maintain. Also, thermalization, the required mechanism to transport electrical signals to the quantum processor from RT instruments, becomes cumbersome and complex with the scaling of quantum processors. Therefore, placing interface electronics at an intermediate temperature of 3-4K solves most of these issues, while at the same time facilitating an increase in qubit count.

Cryogenic integrated circuit design, however, brings many additional challenges. Circuits placed inside the dilution refrigerator have to operate with low power consumption, since the absorbing capabilities of the refrigerator are limited to a maximum of 1-2 W at 4K. At the same time, it needs to introduce as little noise as possible so that it keeps fidelity under control. Low power and low noise requirements are usually contradictory in circuit design, thus trade-offs need to be understood and significant optimization is required to achieve the desired properties. To perform this optimization, accurate models of the qubits and the effects of electronic signals on the qubit operations must be considered. The models would allow to analyze the performance of the system and to understand the problems and potential improvements.

In this paper, we present a method for determining the specifications for parameters of the qubit control signals, and cryogenic circuits for qubit control. We show how single gate fidelity and average Clifford gate fidelity obtained from the simulations can be used to define the requirements and to understand the margins of the control signals and circuits. Furthermore, the influence of different signal and qubit parameters on the resulting operation fidelity is analyzed. This approach can be used in the circuit design process to determine whether the designed circuit is compatible with the qubits already before fabrication.

The paper is organized as follows. Section II introduces the Master equation formalism, system Hamiltonians and performance metrics that are used in this work. Section III presents simulation results showing the influence of control signals and qubit parameters to the system performance. Section IV concludes the paper and provides an outlook.

II. Methods

A quantum system coupled to the environment can be described by the Master equation in Lindblad form under the Born-Markov approximation [4]

$$\frac{\partial \rho(t)}{\partial t} = -i[H, \rho(t)] + \gamma_1 \mathcal{D}[a]\rho(t) + 2\gamma_\phi \mathcal{D}[a^\dagger a]\rho(t), \quad (1)$$

where ρ is the density matrix of the system, H is the Hamiltonian, a is an annihilation operator, γ_1 and γ_2 are relaxation and dephasing rates respectively, and $\mathcal{D}[A]\rho$ is the dissipator for an operator A applied to a density matrix ρ, defined as: $\mathcal{D}[A]\rho = A\rho A^\dagger - \frac{1}{2}A^\dagger A\rho - \frac{1}{2}\rho A^\dagger A$. This approach allows treating the effects of the microwave driving signal, its non-idealities and noise in quantum and classical parts of the system

979-8-3503-4859-0/DATE24/© 2024 EDAA

[5], [6]. The Hamiltonian of a transmon qubit in quantum harmonic oscillator basis [7] can be expressed as

$$H = H_{sys} + H_d, \tag{2}$$

where

$$H_{sys} = \omega_q a^\dagger a + \frac{\alpha}{2} a^\dagger a^\dagger a a, \tag{3}$$

and H_d is the Hamiltonian representing capacitive coupling of the drive, as follows:

$$H_d = \Omega_d V_d(t)(a^\dagger - a), \tag{4}$$

where

$$V_d = A(t) cos(\omega_d t + \phi). \tag{5}$$

V_d is a driving signal, with an amplitude function $A(t)$, frequency ω_d and phase ϕ. Ω_d determines the coupling between the driving line and the qubit. Numerically solving (1) with this Hamiltonian can become computationally inefficient because the sampling rate has to be sufficiently high to correctly reconstruct signal V_d, whose frequency is similar to the qubit frequency, which is usually in the GHz, while the sequence duration can be much longer than the period of this signal, or tens or hundreds of μs, depending on the coherence times of the qubit. This issue can be solved in the weak driving case ($\Omega_d << \omega_q$) by moving to the rotating frame and invoking the rotating wave approximation (RWA). The Hamiltonian is transformed according to

$$\hat{H} = UHU^\dagger - iU\frac{dU^\dagger}{dt}, \tag{6}$$

with $U = e^{-i\omega_q t \cdot a^\dagger a}$. After neglecting terms rotating at $2\omega_d$, we obtain the transmon Hamiltonian in the rotating frame with the RWA:

$$H_{sys} = \delta\omega_q a^\dagger a + \frac{\alpha}{2} a^\dagger a^\dagger a a; \tag{7}$$

$$H_d = \frac{\Omega_d A(t)}{2}(cos\phi(a^\dagger + a) + isin\phi(a^\dagger - a)), \tag{8}$$

where $\delta\omega_q = \omega_q - \omega_d$, in this frame, there are no high frequency sinusoidal signals, which relaxes the need for high sampling rates. Equations (7) and (8) are included in the qutip-quantum information processing library flow [8] and (1) is solved using the solvers provided by the library (mesolve). After all the elements of (1) are defined, we can proceed with defining the quantum gates and evaluating the performance of the system.

A. Performance metrics

Performance of the system can be graded based on the single gate fidelity, which is defined as the distance between the actual reached final state ρ and desired final state σ:

$$F(\rho, \sigma) = (tr(\sqrt{\sqrt{\rho}\sigma\sqrt{\rho}}))^2. \tag{9}$$

Similarly, system's performance can be assessed based on the average gate fidelity obtained from the randomized benchmarking protocol (RB). In this sequence, $m-1$ randomly chosen gates from the Clifford group are performed on the qubit and the sequence is inverted by the last gate that projects it to the ground state. For each length this protocol is repeated with different randomly selected sequences of Clifford gates and the resulting ground state population probability is averaged. The ground state probability decays as:

$$F_{seq} = A(1 - \frac{2^N r}{2^N - 1})^m + B, \tag{10}$$

where A and B are constants that absorb state preparation and measurement (SPAM) errors, N is the number of qubits and r is the average error rate per Clifford. The average Clifford gate fidelity in this case is given by $F_{av} = 1 - r$. In the following analysis, we will show how both of these metrics can be used to analyse the impact of different control signal parameters.

III. Results

For the basis of our analysis, we take a transmon qubit with parameters summarized in Table I. Qubits with similar performance are utilized in state-of-the-art multiple qubit systems [9]. In this section we will show simulations of the system performance for different driving signal frequencies, f_d, strengths Ω_d, envelope shape functions $A(t)$, amplitude noise, and in the presence of spurious interfering signals. We consider qubits with 3 states: ground and two excited states, to take into account population leakage. The simulations are compatible with considering more states at the expense of computational time.

A. Control signals influence on gate fidelity

TABLE I
CONSIDERED QUBIT PARAMETERS

Parameter	f_q	α	T_1	T_2
Value	5 GHz	-180 MHz	30 μs	35 μs

We begin by discussing the signal frequency influence. Equation (8) assumes driving the qubit with a signal of a single frequency, driving with frequency non-idealities will be analyzed in Section III-D. By simulating a Rabi Chevron pattern we can see the effects of the driving signal frequency to the Rabi oscillation of the qubit in Fig. 1 a). As expected, the best performance of the π pulse is obtained at resonance with the qubit.

After fixing the driving frequency to be in resonance with the qubit, we can proceed with estimating the driving amplitude Ω_d. As an initial guess of the amplitude function, we use the raised cosine function to firstly determine the driving strength and gate duration before we proceed with the envelope shape analysis. We can evaluate the fidelity of a single gate and the average gate fidelity through RB. For the following analysis we define the RB algorithm simulation similar to [10]. We used Clifford gates from [1] with the identity gate defined as two $X(\pi)$ gates concatenated. This leads to 1.92 physical gates per Clifford. SPAM errors are not considered in this simulation since the goal is to determine how the fidelity depends on different parameters of the control signal. Therefore we can fix $A = B = 0.5$ in (10). On Fig. 1 b) a RB protocol is repeated with different driving amplitudes. The same random sequence is repeated for all amplitudes to eliminate any effects that could

potentially come from the usage of different sequences and isolate the effect of the amplitude. Based on the average gate fidelity an optimal amplitude is determined to be around 15 MHz. For raised cosine amplitude this leads to a π pulse of 66.67 ns. Lower amplitudes result in a single gate duration which is too long and the sequence fidelity is limited by the qubit relaxation (T_1). On the other hand, due to the presence of states outside the computational space, fidelity for the higher amplitudes is limited by the leakage. We can confirm this conclusion by looking at the single X_π pulse fidelity, which is determined from (9). Two fidelity metrics give almost exactly the same result in this case due to the fact that every gate in the RB sequence is influenced in the same way by the change of amplitude. Thus, the behavior of a single gate is simply translated to a full array of gates used in RB and the fact that different sequences and lengths are analyzed does not influence dramatically the end result. By using the single gate fidelity to evaluate the influence of a given effect, we can save computational time.

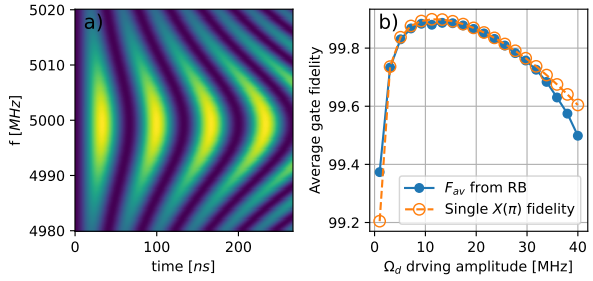

Fig. 1. a) Chevron pattern simulation, b) Driving strength optimization.

Next, we continue with the envelope shape function analysis $A(t)$. Three different options are considered: raised cosine, rectangular and cosine pulses. Ω_d, maximum amplitude is determined in the previous step and is kept constant at 15 MHz. π pulse duration is given by the integral of power and since cosine and raised cosine have a smaller integral over one period, π pulse duration will be longer than in the case of a rectangular pulse shown in Fig.2 inset. Slower gates are more affected by relaxation and dephasing (T_1 and T_2), but still these envelopes give a better fidelity, as seen in Fig.2. This is due to the state leakage, i.e. rectangular pulse delivers more power in a shorter time, thus increasing the probability of populating the second excited state.

Furthermore, we performed a sweep of the qubit anharmonicity and T_1 time and compared the fidelity for different envelopes. Other parameters are kept the same as on Table I, and Ω_d is fixed to 15 MHz. On Fig.2 a) we can see that for α =-180 MHz rectangular envelope gives significantly lower fidelity while the other two have similar performance. For this reason, either cosine or raised cosine envelopes should be used. Moreover, for high values of aharmonicity rectangular pulse fidelity approaches the other two because the probability of exciting higher states becomes low for this pulse also, and the fidelity is no longer limited by this effect. On Fig.2 b) we can see how the fidelity behaves for different T_1 times. From this we can conclude that for the qubit of interest the fidelity is not T_1 limited for a wide range of relaxation times. Clearly, this depends on the value of α and for higher anharmonicity T_1 influence will become visible faster. The drop of fidelity starts at different values of T_1 for the three envelopes, which is due to the π pulse duration. Raised cosine pulse is the longest and the decrease starts at about 10 µs, cosine at about 8 µs and rectangular at 4.5 µs. This gives rise to an interesting regime in which the fidelity is entirely limited by T_1 and the rectangular envelope offers the best performance, for $T_1 <\sim$2.5 µs. Based on this analysis we can say that it is important for the cryogenic control to be able to generate different pulse envelopes in order to guarantee that we can extract maximum possible performance from the qubit. In multiple qubit systems different qubits might also require different envelopes for best performance, so it is important that the control allows for modifying this dynamically during system operation. For investigation of other parameters of the signal we selected the raised cosine envelope.

Red dots on Fig.2 represent average fidelity results from RB simulation. Good agreement between two fidelities is probably because each gate in the sequence is altered in the same way by the anharmonicity and T_1, similar to the case of Ω_d on Fig.1.

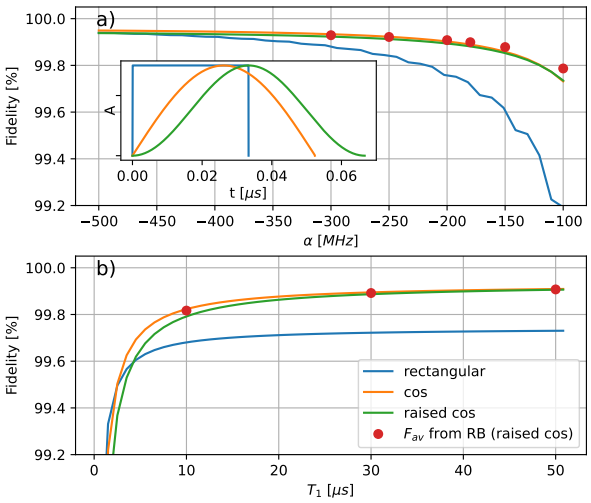

Fig. 2. a) Single gate fidelity vs. qubit anharmonicity, other parameters are like in Table I, b) Single gate fidelity vs. T_1, no dephasing is assumed and other parameters are like in Table I, Inset- Single π pulse for different envelope shapes.

B. Amplitude noise influence on gate fidelity

Influence of the arbitrary white Gaussian noise (AWGN) present on the control signal amplitude can be simulated by adding a zaro-mean Gaussian distributed random variable $\delta\Omega$ to the amplitude. In this case we have $\Omega_d(t) = \Omega_{d0}(t) + \delta\Omega$ where Ω_{d0} is an ideal noiseless amplitude. Fig. 3 inset shows an example of a single gate control signal with a noisy amplitude. Evaluating the fidelity of a single gate in this case requires averaging over multiple iterations of noise traces, because the noise is introduced through a random variable. After averaging

we can see the trend of decreasing fidelity with noise standard deviation increase, as seen in Fig.4. The average fidelity from RB already contains averaging, therefore no modifications to the described RB procedure are needed. Fig. 3 shows the RB sequence simulation for three different noise strengths; each point in the plot is obtained by averaging over 10 different random sequences. Noise level is characterized by the σ-standard deviation of the amplitude and is given in percentage of the maximum drive amplitude. From Fig. 3 we can conclude that for the analyzed qubit the instability of the control amplitude needs to be kept below 1% to reach the average fidelity per Clifford gate above 99.9%, if raised cosine pulses are used and the gate $X(\pi)$ duration is 66.67 ns.

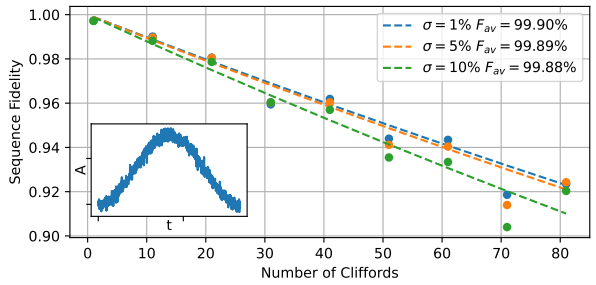

Fig. 3. Average gate fidelity with different noise strengths on the control signal amplitude. Inset- Example of the single noisy gate control signal.

By calculating the average Clifford fidelity at other standard deviations of noise, we can see that the fidelity trend is similar for both the single gate averaged over multiple noise traces and average Clifford fidelity. This can be seen in Fig.4. Similarly to the previously analyzed parameters, the length of the sequence does not change the fidelity drop dramatically. The errors due to noise on an isolated gate are just transferred to the whole sequence, therefore, amplitude noise effect can also be estimated based on the averaged single gate fidelity.

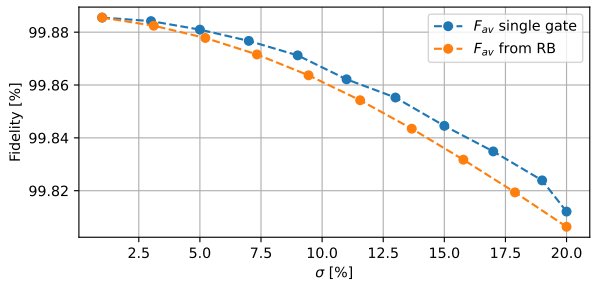

Fig. 4. Gate fidelity dependence on the standard deviation of noise.

C. Simulating Dephasing effects

Qubit dephasing is due to uncontrolled fluctuations of the qubit transition frequency, which is caused by different noise sources present in the environment [11]. Dephasing time is usually measured by a Ramsey sequence, consisting of two $\pi/2$ pulses separated by a waiting time. In the presence of dephasing as the waiting time grows, phase information is lost and the measurement results in a decaying probability of detecting excited state. Modeling dephasing is of interest, since it can limit the gate fidelity and change the specifications for the control circuits. In Lindblad Master equation (1) dephasing is introduced through γ_ϕ and operator $a^\dagger a$ [12]. If $\rho_{ab} = \langle a| \rho |b\rangle$ is a matrix element of the density operator of the qubit and a and b represent qubits states. It can be shown that the phase of the ground-excited state transition will behave as:

$$\rho_{ge}(t) = \rho_{ge}(0)exp(-(\frac{\gamma_1}{2} + \gamma_\phi)t) = \rho_{ge}(0)exp(-\frac{t}{T_2}), \quad (11)$$

with the decay time T_{2exp} defined as:

$$T_{2exp} = \frac{1}{\frac{\gamma_1}{2} + \gamma_\phi}. \quad (12)$$

From (11), phase information, and thus Ramsey sequence will decay exponentially with time. However, in some cases, probably due to the presence of $1/f$ noise, a Gaussian decay of the Ramsey sequence is observed [13]. This can be modelled by changing the dephasing operator and adjusting the dephasing rate. It can be shown that for a dephasing operator $a^\dagger a\sqrt{t}$ the decay and resulting $T_{2gaussian}$ will be the following:

$$\rho_{ge}(t) = \rho_{ge}(0)exp(-\frac{\frac{\gamma_1}{2} + \gamma_\phi}{2}t^2) = \rho_{ge}(0)exp(-(\frac{t}{T_2})^2), \quad (13)$$

$$T_{2gaussian} = \sqrt{\frac{2}{\frac{\gamma_1}{2} + \gamma_\phi}}. \quad (14)$$

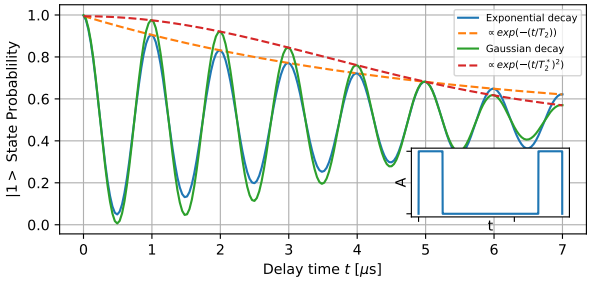

Fig. 5. Ramsey pattern with $T_{2exp} = T_{2gauss} = 5$ µs. Inset-Ramsey sequence control signal amplitude vs. time, two $X(\pi/2)$ gates separated by the delay time.

In this way dephasing becomes time-dependent, which is in agreement with the assumption that $1/f$ noise is the reason for observing a Gaussian decay. With the increasing of the duration of interest, the frequency bandwidth increases towards low frequencies and the influence of $1/f$ noise is therefore increased. Similarly in the model of (13), as the time increases, the dephasing rate also increases. To test the model, we select a qubit which is clearly limited by dephasing by shortening the T_2, from Table I, to 5 µs.

Two different definitions of the dephasing operators and decay times lead to Ramsey patterns behaving as expected Fig. 5. However, simulating extended waiting periods directly using (8) is inefficient. During the wait time, when there is no driving signal and $\delta\omega_q$ becomes equal to ω_q. Thus, employing

a small time step for the simulation is necessary. In the Bloch sphere picture the absence of the driving will result in the qubit precession around the z-axis. However, exact precession is not important for the final state estimation and it is enough to keep track of the phase that qubit accumulates during this period.

Accumulated phase $\phi = \omega_q t_{wait}$ can be included in (8) for the $X(\pi/2)$ gate, which follows the wait time, thus rotating the frame to take into account that the qubit was precessing during the waiting time. This approach maintains reasonable step sizes, thus preventing an increase in simulation duration; yet it adequately captures the qubit precession effect through the accumulated phase. The complete simulation of the sequence in Fig. 5 took approximately 5 minutes with 200 waiting time steps.

Finally, different shapes of phase decay result in a different average gate fidelity obtained from the Randomized benchmarking. This leads to different requirements for the control electronics of the qubits, which experience exponential and Gaussian dephasing, as seen in Fig. 6, and shows the importance of using the correct dephasing model for deriving the requirements for a particular qubit.

Single gate fidelity, calculated with (9), in this case gives 99.8% for the exponential case and 99.88% for Gaussian case. The discrepancy in the results between this and the RB average fidelity comes from the fact that dephasing during a gate affects the subsequent gate more than the single gate itself. Because of this cumulative effect, the fidelity of the sequence is different from the single gate fidelity. Also, Gaussian dephasing does not affect every gate in the sequence in the same way, due to dephasing operator now being time dependent. The gates that are later in the sequence will be more affected. For this reason, the fidelity obtained from the RB in this case should be more realistic.

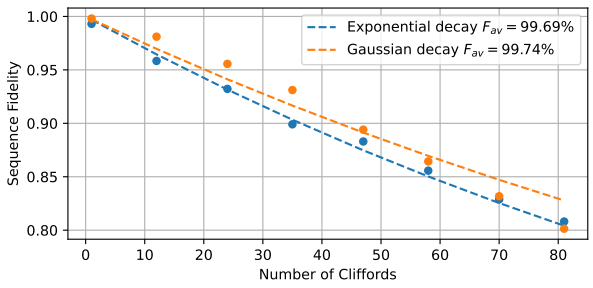

Fig. 6. Randomized benchmarking for Gaussian and Exponentially decaying qubit phase with $T_{2exp} = T_{2gauss} = 5$ µs. Other qubit parameters are the same as in Table I.

D. Non-ideal driving frequency effects

Driving signal defined in (15) assumes that the qubit is driven with the single frequency ω_d. However, in real setups there might be other spurious interfering signals. Driving signal with one interfering spurious tone becomes:

$$V_d = A(t)cos(\omega_d t + \phi) + A_2(t)cos(\omega_2 t + \phi_2), \qquad (15)$$

where A_2, ω_2 and ϕ_2 are amplitude, frequency and phase of the interfering signal, respectively. Now, transforming the new Hamiltonian to the rotating frame (6) and applying the RWA gives:

$$H_d = \frac{\Omega_d}{2}\left(A_1(t)cos\phi + A_2(t)cos(\delta_2 t + \phi_2)\right)(a^\dagger + a) + \\ + i(A_1(t)sin\phi + A_2(t)sin(-\delta_2 t + \phi_2))(a^\dagger - a), \qquad (16)$$

with $\delta_2 = \omega_2 - \omega_d$ being the difference between the two frequencies. Using (16) we can estimate the influence of the spurious tones on the gate fidelity and understand how it evolves with frequency and second tone amplitude. The second tone can represent a characteristic of a non-ideal spectrum of the oscillator, which is used to generate the control signals. By this simulation, we may get an estimation of the spurious free dynamic range (SFDR) of the control circuits that can be tolerated in the system.

In this analysis we assume that the envelope shape of the first and second tone are the same. This assumption is reasonable, considering that both tones originate from the same signal source and that the envelope shape is applied after the frequencies are generated [14]. Also, since the second tone is uncontrolled, we assume that the phase difference between the first and the second tone $\phi - \phi_2$ is also uncontrolled and that the second tone can have a random phase with respect to the first one. For this reason, the fidelity of a single gate in this case is averaged over multiple iterations.

Finally, all gates are influenced in a similar way by the second frequency and the effect of this non-ideality does not depend on the length of a sequence or a position of a particular gate in the sequence. Therefore, single gate fidelity and RB fidelity give simiar results.

Fig.7 shows a sweep of the second tone frequency with its amplitude fixed to 1% of the main tone amplitude. As expected, the fidelity drops if the second frequency is close to the qubit frequency, because in that case the qubit is effectively driven by both tones leading to an over rotation. This effect is also visible on the Chevron pattern, seen in Fig.1 a). The sensitivity of the qubit to the driving of the second tone drops significantly after it is more than ~ 30 MHz far from the qubit. Fig.7 shows another drop in fidelity as the frequency approaches -180 MHz. This happens because the second excited state population probability increases. At this frequency we have the case where the first tone is driving the $0-1$ resonance, while the second one is driving the $1-2$ transition. This leads to an increased leakage and the fidelity drops.

Finally, on Fig.7 we can see that the drops of fidelity happen on the same frequencies in both single qubit and RB case, the difference between the two is below 0.03%, and the estimated decrease is similar. Sweep of the second tone power also shows similar difference between the two fidelities, shown in Fig.8.

Furthermore, we can investigate the sensitivity of the fidelity to the power of the interfering tone. On Fig.8 we show the fidelity trend with changing the SFDR considering that the spurious frequency is in one case at -100 MHz and in the other at -180 MHz from the main tone which is in resonance with the qubit. -100 MHz frequency is far from both $0-1$ and $1-2$ transitions of the qubit and the average fidelity has a weak

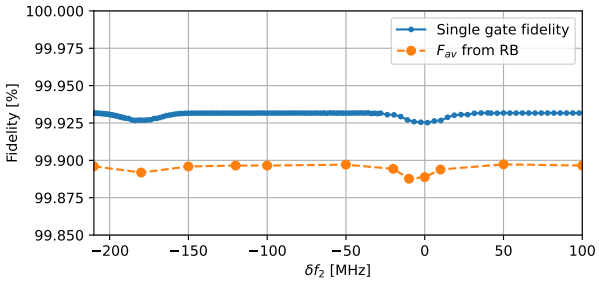

Fig. 7. Second frequency sweep for $A_2/A_1 = 0.01$.

dependence on power. All frequencies, which are not near the qubit transitions show similar trends. At these frequencies, the qubit is not sensitive, and even relatively high power does not influence the perfomance. However, tones which are close to either the $0-1$ or $1-2$ transition show significant dependance on power. From Fig.8 we can conclude that a SFDR lower than 30-35 dBc for -180 MHz leads to an important drop in fidelity for the considered qubit. Similar behavior is also observed for the frequencies closer than 30 MHz to the $0-1$ resonance.

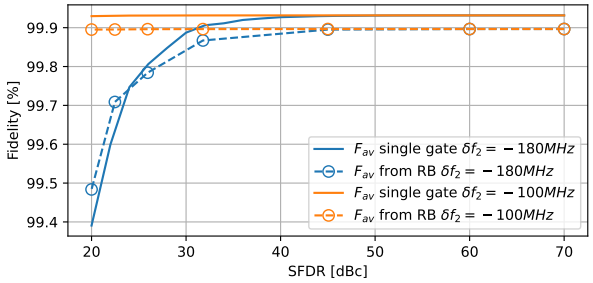

Fig. 8. Fidelity vs. SFDR for two different spurious tone frequencies.

IV. Conclusions

In this paper, we have proposed methods to evaluate the influence of non-idealities of control signals that are used to drive qubits. The goal is to derive specifications for classical control circuits operating at cryogenic temperatures, so as to streamline their design and reduce development time.

We have provided a case study based on state of the art multiple qubit system to explore the effects of different parameters both in the quantum and classical parts of the system. Specifications for envelope shapes, drive amplitudes, SFDR, qubit coherence and anharmonicity, and amplitude noise have been derived, using our methods, so as to achieve a predetermined gate fidelity.

We have shown how evaluating a single gate fidelity gives similar results as RB average fidelity for many considered parameters. Finally, it is shown how dephasing models can be modified to obtain both Gaussian and exponential decaying phase.

These findings have been illustrated through a number of results, often discussing many trade-offs relevant to designers, and guidance for future scalable system design.

Acknowledgment

The authors wish to thank Antoine Pintart, Gilles-Henry Moreillon and Romain Pythoud for work on the simulations.

References

[1] R. Barends *et al.*, "Superconducting quantum circuits at the surface code threshold for fault tolerance," *Nature*, vol. 508, pp. 500–3, 04 2014.

[2] E. Charbon *et al.*, "Cryo-cmos for quantum computing," in *2016 IEEE International Electron Devices Meeting (IEDM)*, 2016, pp. 13.5.1–13.5.4.

[3] E. Charbon, F. Sebastiano, M. Babaie, A. Vladimirescu, M. Shahmohammadi *et al.*, "15.5 cryo-cmos circuits and systems for scalable quantum computing," in *2017 IEEE International Solid-State Circuits Conference (ISSCC)*, 2017, pp. 264–265.

[4] A. Blais, A. Grimsmo, S. Girvin, and A. Wallraff, "Circuit quantum electrodynamics," *Reviews of Modern Physics*, vol. 93, 05 2021.

[5] R. Acharya *et al.*, "Circuit models for the co-simulation of superconducting quantum computing systems," in *2021 Design, Automation Test in Europe Conference Exhibition (DATE)*, 2021, pp. 968–973.

[6] B. Gys *et al.*, "Circuit model for the efficient co-simulation of spin qubits and their control readout circuitry," in *ESSDERC 2021 - IEEE 51st European Solid-State Device Research Conference (ESSDERC)*, 2021, pp. 63–66.

[7] P. Krantz, M. Kjaergaard, F. Yan, T. P. Orlando, S. Gustavsson, and W. D. Oliver, "A quantum engineer's guide to superconducting qubits," *Applied Physics Reviews*, vol. 6, no. 2, p. 021318, 2019.

[8] B. Li *et al.*, "Pulse-level noisy quantum circuits with QuTiP," *Quantum*, vol. 6, p. 630, Jan. 2022.

[9] S. Krinner *et al.*, "Realizing repeated quantum error correction in a distance-three surface code," *Nature*, vol. 605, no. 7911, p. 669–674, May 2022.

[10] T. Hangleiter, P. Cerfontaine, and H. Bluhm, "Filter-function formalism and software package to compute quantum processes of gate sequences for classical non-markovian noise," *Phys. Rev. Research*, vol. 3, p. 043047, Oct 2021.

[11] J. Bylander *et al.*, "Noise spectroscopy through dynamical decoupling with a superconducting flux qubit," *Nature Physics*, vol. 7, pp. 565–570, 05 2011.

[12] D. A. Lidar, "Lecture notes on the theory of open quantum systems," 2020.

[13] A. Somoroff, Q. Ficheux, R. A. Mencia, H. Xiong, R. Kuzmin, and V. E. Manucharyan, "Millisecond coherence in a superconducting qubit," *Phys. Rev. Lett.*, vol. 130, p. 267001, Jun 2023.

[14] J. P. G. Van Dijk *et al.*, "A scalable cryo-cmos controller for the wideband frequency-multiplexed control of spin qubits and transmons," *IEEE Journal of Solid-State Circuits*, vol. 55, no. 11, pp. 2930–2946, 2020.